Anal. Chem. **2010,** *82,* 3487–3499

Theory of Mid-infrared Absorption Microspectroscopy: II. Heterogeneous Samples

Brynmor J. Davis,[†] P. Scott Carney,[‡] and Rohit Bhargava*[,†]

Department of Bioengineering, Department of Electrical and Computer Engineering, and the Beckman Institute for Advanced Science and Technology, University of Illinois at Urbana−Champaign, Urbana, Illinois 61801

Fourier transform infrared (FT-IR) spectroscopic imaging combines the specificity of optical microscopy with the spectral selectivity of vibrational spectroscopy. There is increasing recognition that the recorded data may be dependent on the optical configuration and sample morphology in addition to its local material spectral response, but a quantitative framework for predicting such dependence is lacking. Here, a theory is developed to relate recorded data to the spectral and physical properties of heterogeneous samples. The modeling approach combines optical theory through rigorous coupled wave analysis with modeling of sampling geometry and sample structure. The interplay of morphology and dispersion are systematically explored using increasingly sophisticated samples to illustrate the dependence of the detected optical intensity on the spatial sample structure. Predictions of spectral distortions arising from the sample structure are quantified, and experimental validation of the developed theory is performed using a microfabricated standard from a commercial photoresist polymer. The developed framework forms a basis for understanding sample induced distortions in spectroscopic IR microscopy and imaging.

Fourier transform infrared (FT-IR) spectroscopic imaging is a rapidly emerging technology that combines the spatial specificity of optical microscopy with the chemical selectivity of vibrational spectroscopy.[1−4] It is commonly misconceived that FT-IR imaging is a simple extension of conventional infrared spectroscopy using a different sampling accessory, namely a microscope. From the optics perspective, similarly, it is tempting to conclude that FT-IR imaging is an extension of optical microscopy with discrimination of IR light by wavelength. In this series of articles, it is shown that neither characterization is accurate. In the previous article,[5] optical theory for IR microscopy was developed and it was demonstrated that the combination of the sample−substrate structure and optical configuration can result in significant distortions in data recorded from homogeneous samples. Briefly, optical theory was applied to model interrogation of a sample that was assumed to consist of a homogeneous layer in a sample−substrate structure with no transverse variation. The sample was characterized by upper and lower boundaries and by the frequency dependent complex relative permittivity $\varepsilon(\bar{\nu})$, or equivalently, by a constant complex refractive index.

In this article, the analysis is extended to heterogeneous samples that vary in the lateral sample plane. The sample is characterized by upper and lower boundaries as well as a transverse structure defined by permittivity, $\varepsilon(x, y, \bar{\nu})$. An example of this type of structure is shown in Figure 1. While the sample has nontrivial structure in the imaging plane, it is assumed to be piecewise constant as a function of depth. Such a model is appropriate for thin samples as are usually encountered in IR microspectroscopy. This structure is amenable to analysis through coupled wave theory. The notation used here is consistent with the first article[5] and is also listed in the glossary of Table S1 in the Supporting Information.

In the earliest studies,[6] it was noted that heterogeneous sample structure distorts both the apparent spectrum and the apparent spatial structure in FT-IR imaging. Other authors have also attributed spectral distortions to heterogeneous sample structure.[7−9] While experiments[10] demonstrated that distortions arose from a mismatch of refractive index between domains in the sample, a complete theoretical model to predict the effects of heterogeneous samples on observed spectra and spatial structure has not been presented. The absence of such a model can lead to misinterpretation of spatial structure and/or spectral changes observed at the boundaries of domains. The full analytical capability of FT-IR imaging can only be realized through proper modeling of the optical physics of the combined sample-instrument system. These models help, first, to understand the true spectral and structural content of the data. Second, they help provide measures of the systematic error due to distortions. Studies that claim chemical

* To whom correspondence should be addressed. E-mail: rxb@illinois.edu.
† Department of Bioengineering and the Beckman Institute.
‡ Department of Electrical and Computer Engineering and the Beckman Institute.

(1) *Spectrochemical Analysis Using Infrared Multichannel Detectors*; Bhargava, R., Levin, I. W., Eds.; Sheffield Analytical Chemistry Series; Wiley-Blackwell: Oxford, U.K., 2005.
(2) Colarusso, P.; Kidder, L. H.; Levin, I. W.; Fraser, J. C.; Arens, J. F.; Lewis, E. N. *Appl. Spectrosc.* **1998**, *52*, 106A–120A.
(3) Levin, I. W.; Bhargava, R. *Annu. Rev. Phys. Chem.* **2005**, *56*, 429–474.
(4) Lewis, E. N.; Treado, P. J.; Reeder, R. C.; Story, G. M.; Dowrey, A. E.; Marcott, C.; Levin, I. W. *Anal. Chem.* **1995**, *67*, 3377–3381.
(5) Davis, B. J.; Carney, P. S.; Bhargava, R. *Anal. Chem.* DOI: 10.1021/ac902067p.
(6) Bhargava, R.; Wang, S.-Q.; Koenig, J. L. *Macromolecules* **1999**, *32*, 8989–8995.
(7) Budevska, B. O. *Vib. Spectrosc.* **2000**, *24*, 37–45.
(8) Mohlenhoff, B.; Romeo, M.; Diem, M.; Wood, B. R. *Biophys. J.* **2005**, *88*, 3635–3640.
(9) Bassan, P.; Byrne, H. J.; Bonnier, F.; Lee, J.; Dumas, P.; Gardner, P. *Analyst* **2009**, *134*, 1586–1593.
(10) Bhargava, R.; Wang, S.-Q.; Koenig, J. L. *Appl. Spectrosc.* **1998**, *52*, 323–328.

10.1021/ac902068e
Published on Web 04/14/2010

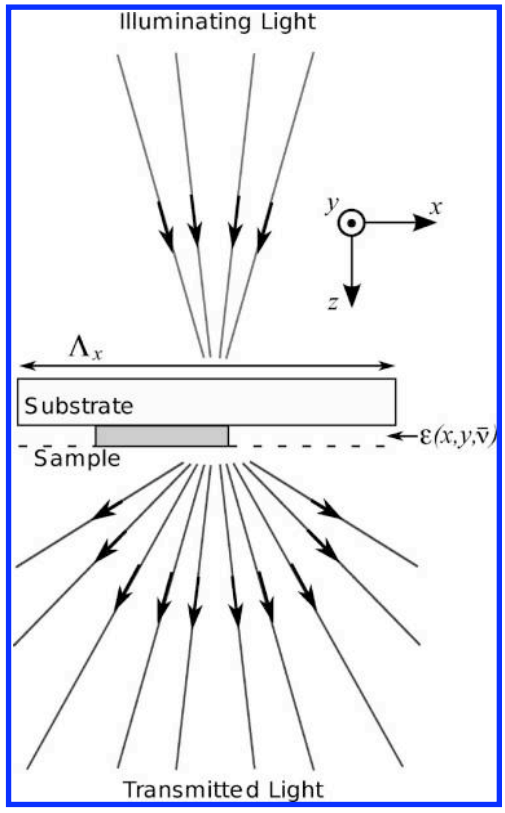

Figure 1. An illustration of the type of sample and substrate geometry considered in this article. Here the sample (a slab of finite extent) is illuminated through a substrate. The sample layer is defined by the permittivity $\varepsilon(x, y, \bar{v})$, and the region of interest is of width Λ_x in the x direction. In contrast to the previous article, the sample may scatter light outside of the illumination angles.

or structural changes at edges of domains might employ the model reported here to verify that the magnitude of those changes is indeed larger than those due to optical effects alone. In this article, optical theory for analysis of heterogeneous structures in mid-IR imaging is developed. The variation of certain parameters in the model is predicted to lead to specific distortions. Predictions are compared to experimental data.

THEORETICAL MODEL

In the preceding work,[5] it was shown that each planewave mode of the electric field (indexed by the propagation directions s_x and s_y) may be propagated through the sample−substrate system independently. When transverse sample structure is introduced this is no longer true. Optical effects such as scattering and refraction induce coupling between the modes. These effects are calculated below using rigorous coupled wave analysis,[11−13] which was originally developed for modeling diffraction gratings. While there are alternative methods which could be used to solve the problem at hand,[14−16] coupled wave analysis provides a clear description of how the transverse structure of the object couples planewave modes. The coupled wave method is also widely used, and the associated numerical implementation is well studied.[17] In the following presentation, rigorous coupled wave analysis is briefly described and applied to the mid-IR imaging problem in order to explain artifacts, for example, from edge scattering.

It is assumed that the transverse area of interest in the sample is some finite range $\Lambda_x \times \Lambda_y$ in Cartesian coordinates x, y. The object within this range can then be represented in the Fourier series

$$\varepsilon(x, y, \bar{v}) \approx \sum_{p=-N_U}^{N_U-1} \sum_{q=-N_W}^{N_W-1} \phi_{p,q}(\bar{v}) \exp[i(pUx + qWy)] \quad (1)$$

where $U = 2\pi/\Lambda_x$ and $W = 2\pi/\Lambda_y$. The Fourier series has been truncated to $2N_U$ terms in the x direction and by $2N_W$ terms in the y direction. Note that this representation repeats the object periodically outside the region of interest. However, the problem is formulated below so that light is focused into the single period $\Lambda_x \times \Lambda_y$ with negligible intensity outside this area.

The reciprocal of the permittivity is well-defined and will be useful in the analysis below. This function can also be represented as the Fourier series,

$$[\varepsilon(x, y, \bar{v})]^{-1} \approx \sum_{p=-N_U}^{N_U-1} \sum_{q=-N_W}^{N_W-1} \psi_{p,q}(\bar{v}) \exp[i(pUx + qWy)] \quad (2)$$

As with the first article,[5] the incident field is decomposed into a collection of constituent planewaves. Each individual planewave component is infinite in extent and thus impinges on the periodic extension of the sample structure. A localized response is generated by summing over the planewave spectra near the end of the calculation, but for intermediate steps, it is useful to be able to appeal to the formal periodicity.

Consider an incident planewave with Cartesian transverse spatial frequency components δ and σ, that is, a field proportional to $\exp[i(\delta x + \sigma y)]$ in a fixed z plane. The spatial periodicity of the sample implies that the scattered field consists only of planewave components with transverse spatial frequencies that are shifted from those of the incident field by integer multiples of the constants, U and W. Explicitly,

$$u_p = pU + \delta \quad (3)$$

$$w_q = qW + \sigma \quad (4)$$

That is, through interacting with the sample, an incident planewave with transverse frequencies δ and σ must give rise to planewaves with transverse dependence of the form $\exp[i(u_p x + w_q y)]$, due to the translational periodicity of the problem. At $p = q = 0$, the undiffracted component is obtained and all other values represent diffracted modes.

For reasons similar to those given above, the field in any fixed-z plane of the sample must be composed of fields with the same

(11) Moharam, M. G.; Gaylord, T. K. *J. Opt. Soc. Am.* **1981**, *71*, 811–818.
(12) Moharam, M. G.; Gaylord, T. K. *J. Opt. Soc. Am.* **1983**, *73*, 1105–1112.
(13) Gaylord, T. K.; Moharam, M. G. *Proc. IEEE* **1985**, *73*, 894–937.
(14) Li, L. *J. Opt. Soc. Am. A* **1996**, *13*, 1024–1035.
(15) Li, L. *J. Opt. Soc. Am. A* **1997**, *14*, 2758–2767.
(16) Jin, J. *The Finite Element Method in Electromagnetics*, 2nd ed.; Wiley-IEEE Press: New York, 2002.
(17) Moharam, M. G.; Grann, E. B.; Pommet, D. A.; Gaylord, T. K. *J. Opt. Soc. Am. A* **1995**, *12*, 1068–1076.

transverse frequencies given in eqs 3 and 4. Therefore, in the sample layer (indexed by layer $\ell = \Delta$), between $z^{(\Delta-1)}$ and $z^{(\Delta)}$, the electric field vector can be written in the form

$$\mathbf{E}^{(\Delta)}(x,y,z,\bar{\nu}) = \sum_p \sum_q \begin{bmatrix} X_{p,q}(z,\bar{\nu}) \\ Y_{p,q}(z,\bar{\nu}) \\ Z_{p,q}(z,\bar{\nu}) \end{bmatrix} \exp[i(u_p x + w_q y)] \tag{5}$$

Note that while the Fourier transform of the object function was truncated in eq 1, the field resulting from scattering from this approximation to the object need not be similarly band-limited. However, it is necessary in the numerical calculation of $\mathbf{E}^{(\Delta)}(x, y, z, \bar{\nu})$ to make a potentially different truncation of eq 5. This truncation is made such that the diffracted-field coefficients $X_{p,q}(z, \bar{\nu})$, $Y_{p,q}(z, \bar{\nu})$, and $Z_{p,q}(z, \bar{\nu})$ have decayed to a negligible level before the truncation point.

In the inhomogeneous sample layer, the magnetic field is nontrivially related to the electric field (c.f., the relationship in a homogeneous layer[18]). Hence it will be convenient to describe the magnetic field separately as

$$\mathbf{H}^{(\Delta)}(x,y,z,\bar{\nu}) = \sqrt{\frac{\varepsilon_0}{\mu_0}} \sum_p \sum_q \begin{bmatrix} I_{p,q}(z,\bar{\nu}) \\ J_{p,q}(z,\bar{\nu}) \\ K_{p,q}(z,\bar{\nu}) \end{bmatrix} \exp[i(u_p x + w_q y)] \tag{6}$$

In the homogeneous layers, e.g., in the substrate or in the homogeneous sample addressed in the preceding article, each component of the planewave spectrum of the field can be propagated independently and the results can be summed to find the field at any given plane.[19] In the structured sample considered here, the relationship between fields in distinct transverse planes is more complicated and this is reflected in the very general dependence of eqs 5 and 6 on z. The evolution of the electric and magnetic fields with z is found using the Maxwell−Faraday equation and Ampère's circuital law. With the use of the time harmonic form and the fact that $c = 1/(\varepsilon_0\mu_0)^{1/2}$, these can be written

$$\nabla \times \mathbf{E}(\mathbf{r},\bar{\nu}) = i2\pi\bar{\nu}\sqrt{\frac{\mu_0}{\varepsilon_0}}\mathbf{H}(\mathbf{r},\bar{\nu}) \tag{7}$$

$$\nabla \times \mathbf{H}(\mathbf{r},\bar{\nu}) = -i2\pi\bar{\nu}\varepsilon(\mathbf{r},\bar{\nu})\sqrt{\frac{\varepsilon_0}{\mu_0}}\mathbf{E}(\mathbf{r},\bar{\nu}) \tag{8}$$

Substituting eqs 5 and 6 into eq 7 and equating coefficients for each transverse frequency pair (u_p, w_q) results in the equations

$$\frac{\mathrm{d}X_{p,q}(z,\bar{\nu})}{\mathrm{d}z} = i2\pi\bar{\nu}J_{p,q}(z,\bar{\nu}) + iu_p Z_{p,q}(z,\bar{\nu}) \tag{9}$$

$$\frac{\mathrm{d}Y_{p,q}(z,\bar{\nu})}{\mathrm{d}z} = -i2\pi\bar{\nu}I_{p,q}(z,\bar{\nu}) + iw_q Z_{p,q}(z,\bar{\nu}) \tag{10}$$

(18) Equation 2 in ref 5.
(19) Equation 4 in ref 5.

$$K_{p,q}(z,\bar{\nu}) = \frac{1}{2\pi\bar{\nu}}[u_p Y_{p,q}(z,\bar{\nu}) - w_q X_{p,q}(z,\bar{\nu})] \tag{11}$$

Substituting eqs 1, 5, and 6 into eq 8 and equating transverse frequency pairs for the x and y components of the vector equation gives the equations

$$\frac{\mathrm{d}I_{p,q}(z,\bar{\nu})}{\mathrm{d}z} = -i2\pi\bar{\nu}\sum_{p''}\sum_{q''}\phi_{p-p'',q-q''}(\bar{\nu})Y_{p'',q''}(z,\bar{\nu}) + iu_p K_{p,q}(z,\bar{\nu}) \tag{12}$$

$$\frac{\mathrm{d}J_{p,q}(z,\bar{\nu})}{\mathrm{d}z} = i2\pi\bar{\nu}\sum_{p''}\sum_{q''}\phi_{p-p'',q-q''}(\bar{\nu})X_{p'',q''}(z,\bar{\nu}) + iw_q K_{p,q}(z,\bar{\nu}) \tag{13}$$

Equating transverse frequency pairs, the z component in eq 8 can be found by first dividing both sides of the equation by $\varepsilon(\mathbf{r}, \bar{\nu})$. The expression for the reciprocal of $\varepsilon(\mathbf{r}, \bar{\nu})$, eq 2, can then be used to give

$$Z_{p,q}(z,\bar{\nu}) = -\frac{1}{2\pi\bar{\nu}}\left\{\sum_{p''}\sum_{q''}\psi_{p-p'',q-q''}(\bar{\nu})[u_{p''}J_{p'',q''}(z,\bar{\nu}) - w_{q''}I_{p'',q''}(z,\bar{\nu})]\right\} \tag{14}$$

The results seen in eqs 9−14 determine how the electric and magnetic fields propagate through the sample layer. The dependence on $K_{p,q}(z, \bar{\nu})$ and $Z_{p,q}(z, \bar{\nu})$ can be eliminated by substituting eq 14 into eqs 9 and 10 and eq 11 into eqs 12 and 13. The result is four sets of coupled first-order differential equations. The (u_p, w_q) frequency pairs retained in eqs 5 and 6 are then placed in a one-dimensional ordering, indexed by m. Using this one-dimensional ordering, each set of functions can be arranged as a $N_F \times 1$ column vector, where N_F is the number of terms retained. These vectors can then be concatenated and the system of differential equations written in the form

$$\begin{bmatrix} \frac{\mathrm{d}\mathbf{X}(z,\bar{\nu})}{\mathrm{d}z} \\ \frac{\mathrm{d}\mathbf{Y}(z,\bar{\nu})}{\mathrm{d}z} \\ \frac{\mathrm{d}\mathbf{I}(z,\bar{\nu})}{\mathrm{d}z} \\ \frac{\mathrm{d}\mathbf{J}(z,\bar{\nu})}{\mathrm{d}z} \end{bmatrix} = i2\pi\bar{\nu}\Phi(\bar{\nu})\begin{bmatrix} \mathbf{X}(z,\bar{\nu}) \\ \mathbf{Y}(z,\bar{\nu}) \\ \mathbf{I}(z,\bar{\nu}) \\ \mathbf{J}(z,\bar{\nu}) \end{bmatrix} \tag{15}$$

where $\Phi(\bar{\nu})$ is a $4N_F \times 4N_F$ matrix. For convenience, the dependence of Φ on $\bar{\nu}$ is suppressed for the remainder of this work.

The form[20] of Φ guarantees that eigenvalues come in pairs of opposite sign, i.e., the eigenvalues of Φ can be denoted by $\pm\gamma_1, \pm\gamma_2, \ldots, \pm\gamma_{2N_F}$. The eigenvectors of Φ are $\mathbf{g}_1, \mathbf{h}_1, \mathbf{g}_2, \mathbf{h}_2, \ldots, \mathbf{g}_{2N_F}, \mathbf{h}_{2N_F}$, where the vector $\mathbf{g}_j$ is associated with the eigenvalue γ_j and the vector $\mathbf{h}_j$ is associated with $-\gamma_j$. The eigenvalue γ_j is taken to lie in the upper half of the complex plane, that is γ_j is chosen such that its imaginary

(20) Equation 57 in ref 17.

part is positive. Note that for purely real eigenvalues, $+\gamma_j$ will be chosen to be positive.

Finding the eigenvalues and eigenvectors of Φ allows the matrix to be decomposed in the form

$$\Phi = G\Gamma G^{-1} \tag{16}$$

where Γ contains the eigenvalues on the diagonal and is zero elsewhere, and the vectors $\mathbf{g}_j$ and $\mathbf{h}_j$ are organized to form the corresponding columns of G.

An uncoupled set of $4N_F$ first order differential equations can be written as a single matrix equation $d\mathbf{V}(z)/dz = i2\pi\bar{\nu}\Gamma\mathbf{V}(z)$, where $\mathbf{V}(z)$ is a $4N_F \times 1$ vector. Such a set of equations is easily solved (each equation can be solved individually) and the result used to construct a solution of eq 15. That solution can be constructed as $G\mathbf{V}(z)$ so that

$$X_m(z,\bar{\nu}) = \sum_{j=1}^{2N_F} \{\beta_j g_{j,m} \exp[i2\pi\bar{\nu}\gamma_j(z - z^{(\Delta-1)})] + \hat{\beta}_j h_{j,m} \exp[-i2\pi\bar{\nu}\gamma_j(z - z^{(\Delta)})]\} \tag{17}$$

$$Y_m(z,\bar{\nu}) = \sum_{j=1}^{2N_F} \{\beta_j g_{j,m+N_F} \exp[i2\pi\bar{\nu}\gamma_j(z - z^{(\Delta-1)})] + \hat{\beta}_j h_{j,m+N_F} \exp[-i2\pi\bar{\nu}\gamma_j(z - z^{(\Delta)})]\} \tag{18}$$

$$I_m(z,\bar{\nu}) = \sum_{j=1}^{2N_F} \{\beta_j g_{j,m+2N_F} \exp[i2\pi\bar{\nu}\gamma_j(z - z^{(\Delta-1)})] + \hat{\beta}_j h_{j,m+2N_F} \exp[-i2\pi\bar{\nu}\gamma_j(z - z^{(\Delta)})]\} \tag{19}$$

$$J_m(z,\bar{\nu}) = \sum_{j=1}^{2N_F} \{\beta_j g_{j,m+3N_F} \exp[i2\pi\bar{\nu}\gamma_j(z - z^{(\Delta-1)})] + \hat{\beta}_j h_{j,m+3N_F} \exp[-i2\pi\bar{\nu}\gamma_j(z - z^{(\Delta)})]\} \tag{20}$$

where $g_{j,m}$ is the mth element of the vector $\mathbf{g}_j$, $h_{j,m}$ is the mth element of the vector $\mathbf{h}_j$, and β_j and $\hat{\beta}_j$ are, as yet undetermined, coefficients. The field in the sample layer is determined by eqs 17−20, with the z-polarized components given by eqs 11 and 14. The sample structure determines the values for γ, $g_{j,m}$, and $h_{j,m}$ through the eigenvalue decomposition of Φ. The $4N_F$ remaining coefficients ($2N_F\beta_j$ coefficients and $2N_F\hat{\beta}_j$ coefficients) are set by boundary conditions, i.e., the illuminating field determines these values.

A representation of the field in the homogeneous layers (e.g., the air surrounding the substrate and sample and the substrate) has been described elsewhere[19] and can be rewritten as

$$\mathbf{E}^{(/)}(x,y,z,\bar{\nu}) = \bar{\nu}\sum_{m=1}^{N_F} \{\mathbf{B}^{(/)}(m,\bar{\nu}) \exp[i2\pi\bar{\nu}s_z^{(/)}(m,\bar{\nu})(z - z^{(/-1)})] + \hat{\mathbf{B}}^{(/)}(m,\bar{\nu}) \exp[-i2\pi\bar{\nu}s_z^{(/)}(m,\bar{\nu})(z - z^{(/)})]\} \times \exp[i(u_{p(m)}x + w_{q(m)}y)] \tag{21}$$

The modes of the field in the homogeneous layers are here indexed by m, whereas in the previous article[5] they were indexed by the transverse propagation quantities s_x and s_y. Writing the modes in the manner above allows the field in the homogeneous layers to be matched to the field in the sample. The relationship between m and s_x and s_y is

$$s_x(m,\bar{\nu}) = \frac{u_{p(m)}}{2\pi\bar{\nu}} = \frac{p(m)}{\Lambda_x\bar{\nu}} + \delta \tag{22}$$

$$s_y(m,\bar{\nu}) = \frac{w_{q(m)}}{2\pi\bar{\nu}} = \frac{q(m)}{\Lambda_y\bar{\nu}} + \sigma \tag{23}$$

where $p(m)$ and $q(m)$ describe the one-dimensional ordering of (p, q) onto m. These equations describe the relationship between the periodicity of the object (Λ_x and Λ_y) and the transverse propagation direction. The axial propagation factor $s_z^{(/)}(m,\bar{\nu})$ is calculated from a dispersion relation.[21] In contrast to the homogeneous layers, at a given transverse spatial frequency, the field in the transversly inhomogeneous sample consists of contributions of different axial propagation constants [compare $s_z^{(/)}(m,\bar{\nu})$ in eq 21 to γ_j in eqs 5, 6, and 17−20].

The field in a homogeneous layer is determined by the vectors $\mathbf{B}^{(/)}(m,\bar{\nu})$ and $\hat{\mathbf{B}}^{(/)}(m,\bar{\nu})$. Just as $4N_F$ coefficients (β_j and $\hat{\beta}_j$) determine the field in the sample layer, transversality conditions[22] reduce the $6N_F$ elements of $\mathbf{B}^{(/)}(m,\bar{\nu})$ and $\hat{\mathbf{B}}^{(/)}(m,\bar{\nu})$ to $4N_F$ independent parameters. Thus, for a sample with L layers, $4LN_F$ parameters fully describe the field. As with the case considered in the preceding article, continuity of the transverse electric and magnetic fields can be enforced at the boundaries for each transverse spatial frequency to give $4(L-1)N_F$ independent constraints. By construction, illumination comes from only one side of the sample so the condition

$$\hat{\mathbf{B}}^{(L)}(m,\bar{\nu}) = \mathbf{0} \tag{24}$$

eliminates another $2N_F$ unknowns. The remaining $2N_F$ parameters are determined by setting the illumination vectors $\mathbf{B}^{(1)}(m,\bar{\nu})$, as described in the first article.[5] The detection of light scattered from the sample is also the same as in the previous article.

For the homogeneous layers considered in the first article, the continuous plane wave spectra[19] could be evaluated numerically by discretizing the transverse propagation cosines s_x and s_y on any grid. In the formulation described here, a natural discrete grid is set by the periodic extension of the object on length scales Λ_x and Λ_y (note that these may be chosen such that the focused light is localized within a single period). This grid may be more coarse than desired, particularly for small values of $\bar{\nu}$. However, the discretization of the incident field in the planewave basis, that is the discretization of (s_x, s_y) in eqs 22 and 23, may be performed for multiple values of (δ, σ). The resulting fields for each value of (δ, σ) may be summed, giving a discretization of (s_x, s_y) on an arbitrarily fine grid, that is at least as fine and commensurate with the descretization dictated by Λ_x and Λ_y.

SIMULATION AND PREDICTION

Numerical simulations are presented here to demonstrate how diffraction and scattering effects in heterogeneous samples are

(21) Equation 5 in ref 5
(22) Equations 6 and 7 in ref 5.

coupled to the sampling geometry, sample morphology, and spectral profile of the sample such that the bulk or so-called "pure phase" spectrum is changed. In the preceding article, it was seen that transmission microspectroscopy is less sensitive to optical distortions than transflection microspectroscopy when a homogeneous layered sample is considered. Further, an overwhelming majority of studies using IR imaging are conducted in the transmission mode.[23] For these reasons, the transmission mode is considered exclusively in the following examples. The extension to transflection is straightforward.

Measurements from two samples are simulated to demonstrate the potential distortions and estimate their magnitude in a first principles manner. In the first example, an object whose response is constant across all wavelengths is considered. Investigation of focused fields in the sample and at the detector illustrates how the spatial structure of the sample affects measurements, independent of the influence of spectral changes. In the second example, full spectral data are simulated for a hypothetical sample of spatially structured toluene, illustrating the increased complexity when spectral variations are added to the sample structure. Effects resulting from the spatial structure of the sample can be seen, and the associated influence on recorded spectra are investigated. In both examples, the effect of an edge on the microspectroscopy data is further investigated. While sensitivity to only the imaginary (absorptive) part of the refractive index is desired, the thickness of the sample and the real part of the refractive index are both seen to affect the data through scattering and diffraction. These effects result in changes in the observed spectral features, including changes in the absorption band profiles and peaks and also changes in the ratios between absorption peaks, which are all quantified.

Frequency-Invariant Sample. In this first example, the sample material considered has no variation in optical response as a function of wavelength. By investigation of the interaction of this sample with focused light of differing wavelengths, some basic behaviors of the microspectroscopy system can be identified. The sample considered is a rectangular slab of absorbing material with index $n = 1.4 + 0.07i$ mounted on a substrate of index 1.45 (i.e., the geometry shown in Figure 1). The slab is 100 μm wide in the x direction and of infinite extent in the y direction, and various thicknesses b in the z direction are considered. The area of interest is taken to be $\Lambda_x = 200$ μm wide in the x direction and infinite in the y direction. The sample is illuminated through the substrate with a y-polarized line-focus. A line-focus is constructed by considering only the $s_y = 0$ line of the aplanatic Cassegrain angular spectrum.[24] A Cassegrain with numerical aperture of 0.5 and a central obscuration aperture of 0.1 is considered. In representing both the object and the field, 200 Fourier series coefficients were retained, i.e., $N_U = N_F = 200$. This level of detail gives sharp edges in the representation of the sample, while increasing the number of Fourier terms did not significantly change the simulation results, indicating that 200 coefficients are sufficient to represent the field. The offsets (δ, σ) were dithered so that there were at least 50 sample points within the numerical aperture of the Cassegrain for all values of $\bar{\nu}$. The angular spectrum from this discretization level leads to a smooth and reasonable focused field.

The line-focus is centered on the absorbing slab in Figure 2. It should be noted that refraction in the substrate has the effect of shifting the nominal focal point.[25] Hence, the sample and substrate have been moved in the axial direction here so that focusing is achieved in the sample plane. This wavelength-dependent (chromatic) shift of the focus has been noted to be a significant problem for dispersive substrates.[25,26] Here it is noted that the substrate also introduces aberration,[25,27] as can be seen by comparing the fields of Figure 2 to fields without a substrate (Figure S1 in the Supporting Information). When the line-focus is positioned between the absorbing slabs, the results of Figure 3 are obtained, while focusing onto the edge of a slab gives the fields shown in Figure 4.

Several comments apply to all three line-focusing cases. Since the sample and illumination have no spatial variation with y and the illuminating light is y-polarized, the field in the sample is also strictly y-polarized. Thus the plots shown are a complete representation of the field. The theory does encompass more general cases, e.g., x-polarized illumination or two-dimensionally focused fields, but the resulting vector fields are more challenging to display. The magnitude of the angular spectrum $B_y^{(3)}(s_x, \bar{\nu})$ is shown in subplots j–l. These spectra can be interpreted as representations of the field strength as a function of direction of propagation. The fine oscillations observed in many of these functions can be attributed to interference between unscattered light and contributions scattered from edges of the slab. Any components of the angular spectrum that lie outside the collection angle of the detection Cassegrain are not collected upon detection. This range is marked by the empty instrument response (i.e., the instrument response with no sample or substrate), in this case $0.1 < |s_x| < 0.5$. Any light diffracted outside the collection range leads to an apparent absorption, as this light is not detected. It should also be noted that any components at $|s_x| > 1$ correspond to waves that are evanescent in free space and do not propagate to the detector. The intensity of light on the detector plane can be calculated from the emerging angular spectra, as described in the previous article.

For illumination focused into the center of the slab, fields within the sample and the transmitted angular spectra are shown in Figure 2. The penetration of the field through the sample is as expected, thicker samples produce more attenuation and longer wavelengths (i.e., lower values of $\bar{\nu}$) are more weakly absorbed. Standing wave effects due to reflection off the top of the sample are also clearly visible. For the thin sample ($b = 2$ μm) it can be seen that there is minimal loss of intensity due to diffraction out of the collection optics, while for thicker samples more light escapes the collection cone. It should be noted that recorded spectra in microspectroscopy are usually of lower signal-to-noise ratio than the bulk recording case. Hence, absorbance of samples is sought to be maximized by adjusting the sample thickness such that the absorbance is maximized in the linear regime of Beer's law. The typical thickness for most samples is 5–10 μm and feature sizes in many composites and biomedical samples are of

(23) Koenig, J. L.; Wang, S.-Q.; Bhargava, R. *Anal. Chem.* **2001**, *73*, 360A–369A.
(24) Figure 4 in ref 5.
(25) Carr, G. L. *Rev. Sci. Instrum.* **2001**, *72*, 1613–1619.
(26) Wetzel, D. L. *Vib. Spectrosc.* **2002**, *29*, 291–297.
(27) Török, P.; Varga, P.; Laczik, Z.; Booker, G. R. *J. Opt. Soc. Am. A* **1995**, *12*, 325–332.

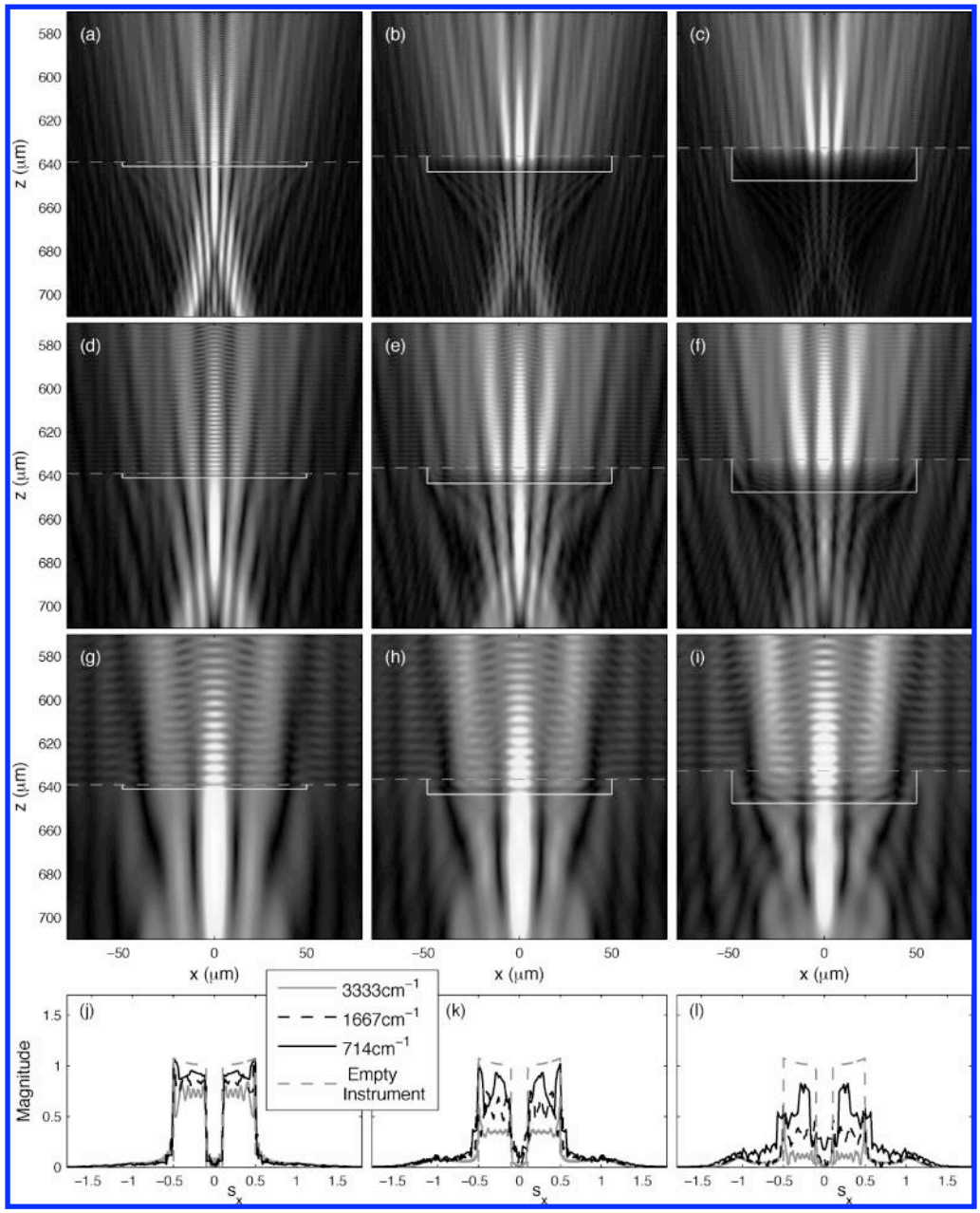

Figure 2. Responses for a line-focused *y*-polarized field incident on the center ($x = 0$) of an absorbing slab. The slab has a complex index 1.4 + 0.07*i* and is mounted on a substrate (the upper region of the plots) of index 1.45 and thickness 2 mm. The field is focused to the $z = 0$ plane in free space. Focusing through the substrate has the effect of moving this focus by about 640 μm, as shown, and also introducing aberration (cf., Figure S1 in the Supporting Information, which considers the same scenario but with the sample suspended in free space). Three sample thicknesses are considered, 2 μm in the left column, 7 μm in the center column, and 15 μm in the right column, that span the usual range in transmission measurements. The *y*-polarized field (the only nonzero field direction) in the sample is shown in parts a−i. The substrate boundary is marked with a dashed line and the slab boundaries with solid lines. Wavelengths of (a−c) 3 μm ($\bar{\nu} = 3333$ cm^{-1}), (d−f) 6 μm ($\bar{\nu} = 1667$ cm^{-1}), and (g−i) 14 μm ($\bar{\nu} = 714$ cm^{-1}) are shown. The magnitude of the angular spectrum after the sample, $B_y^{(3)}(s_x, s_y, \bar{\nu})$ is shown in parts j−l.

a similar order of magnitude. The unfortunate coincidence of order of magnitude for wavelengths, sample features, and optimal path length has an impact on the recorded data for most cases. As this simulation demonstrates, a trade-off between random error and systematic distortion due to optical effects may be avoided in some cases by using thinner samples.

In Figure 3 the same system is considered but with the illuminating light focused between two slabs. There is little light incident on the absorbing material and, apart from a reflection at the substrate boundary, the focused illumination passes through the system largely unperturbed. However, for the thicker samples some scattering effects can be seen in the resulting angular spectra. This illustrates how the optical effects produced by an edge may have a wider region of influence for thicker samples. The implication for a heterogeneous material is that the influence of domains could extend well beyond their obvious morphologic boundaries and proximal regions in a manner that is coupled to the thickness of the sample. While dual aperturing is used in point microspectroscopy to alleviate these effects to some degree, they will be readily apparent in full-field of view imaging.

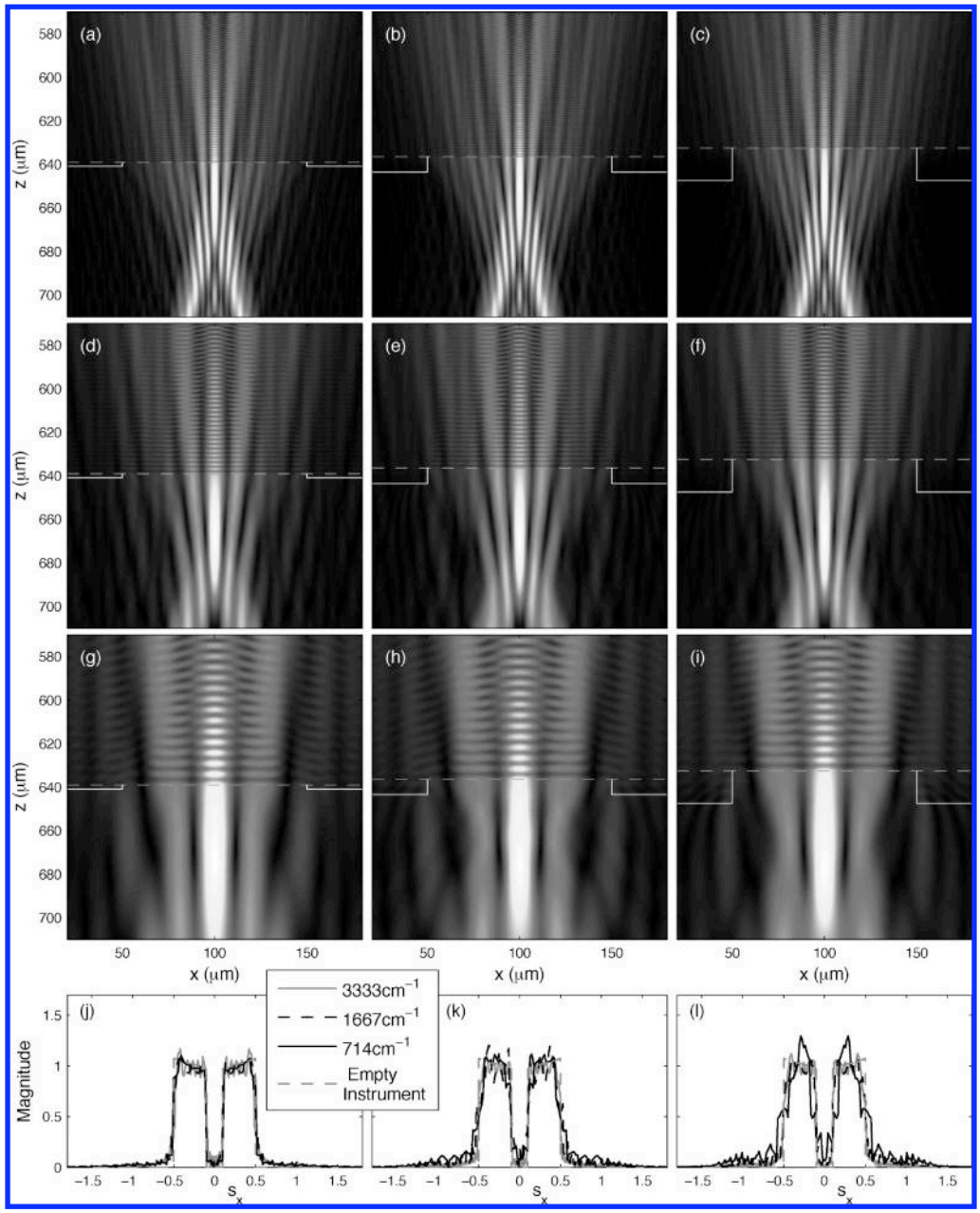

Figure 3. Responses for a line-focused *y*-polarized field incident between two absorbing slabs ($x = 100\ \mu$m) separated by a distance several-fold the wavelength. All other plots and parameters are the same as in Figure 2. A similar scenario, but with the sample suspended in free space, is illustrated in Figure S2 of the Supporting Information.

The illuminating light is focused onto the edge of the sample in Figure 4. In this case, as expected, significant changes to the focused field can be observed. Some of the light is refracted into the absorbing slab and bent out of the collection cone (this can be seen in parts j–l particularly clearly). The resulting sample-induced effects can be seen to trend progressively more prominent with increasing sample thickness. The net effect of an edge is to redistribute spatially the total intensity that would otherwise be incident on the detector. If the distribution is outside of the collection cone, the total intensity reaching the detector is decreased and consequently the apparent absorption is increased. This apparent increase in absorption is only due to optical effects however and depends on the sample morphology. For nonabsorbing spectral regions, the resulting imaging contrast is strong at the edges of domains and is akin to that observed in optical microscopy. The contrast between domains is dictated by their respective refractive indices. While the obvious implication is that an IR microspectrometer may be used in the manner of an optical microscope with properties in the mid-IR region, such a use is not very practical. The primary motivation for working in the mid-IR region is to obtain chemical contrast using absorbance of specific chemical species in spatial domains. Hence, the more important implication is that scattering from nonabsorbing regions of one domain can influence the data recorded in an absorbing spectral region for another domain. In this manner, optical effects complicate data interpretation and make measurements of the spectrum dependent on sample structure.

Animations showing the interactions of the line-focus with the sample are included in the Supporting Information. There is an animation for each combination of wavenumber and sample

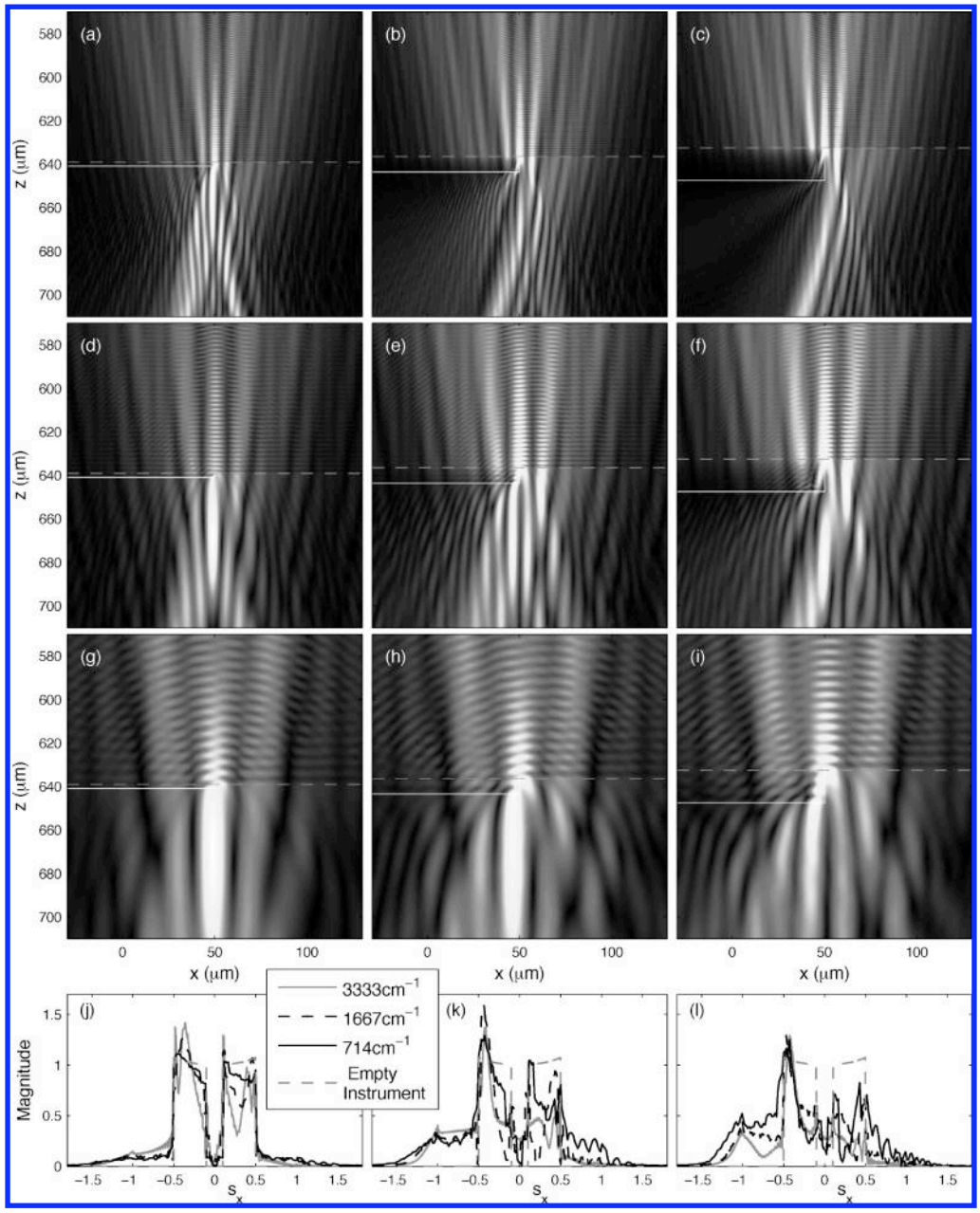

Figure 4. Responses for a line-focused *y*-polarized field incident on the edge ($x = 50\ \mu$m) of an absorbing slab. All other plots and parameters are the same as in Figure 2. A similar scenario, but with the sample suspended in free space, is illustrated in Figure S3 of the Supporting Information.

thickness seen in Figure 2, and a second animation for each combination but with the sample suspended in free space rather than on a substrate.

When the diffracted components are collected, the distribution of light intensity in the detector plane is also affected, meaning that contributions from the edge effects can produce artifacts in pixels besides the ones associated with the edge position. To understand the practical effects of spatial redistribution, a fully two-dimensional focusing solution is needed. Hence, a full focusing aperture, rather than a line-focus, is considered for the remainder of this article. In all cases, circular apertures (as shown in the previous article[24]) are represented on a discrete Cartesian grid, as consistent with the analysis presented in the previous section. The effects of light redistribution are illustrated in Figure 5.

The object from Figure 2 is considered in Figure 5 but represented with $N_U = 40$ coefficients. The angular spectrum of illumination is discretized so that for any wavenumber $\bar{\nu}$ the s_x diameter across the aperture is at least 20 pixels and the s_y diameter is 20 pixels. The field emerging from the sample is represented using an angular spectrum discretized with the same pixel spacing and with 20 pixels in the s_y dimension and at least 60 pixels in the s_x dimension. The discretization described here is more coarse than that used in the previous calculations of the fields in the sample. This is because the predicted detection data are less sensitive to fine features of the field (e.g., evanescent waves) so that the desired prediction ceases to change with the discretization at a more coarse level. The outer and inner Cassegrain numerical apertures are again

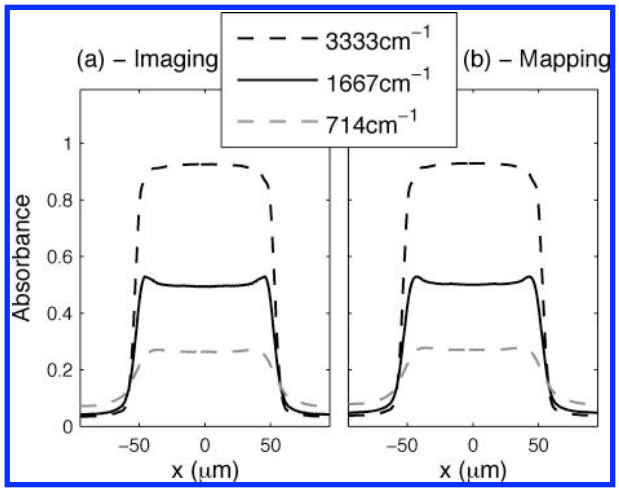

Figure 5. Absorbance profiles of the 7 μm slab of Figure 2, at different wavenumbers and for both (a) imaging and (b) point mapping modalities.

0.5 and 0.1, respectively, which means that the discrete representation of the scattered fields extends well into the evanescent region.

Two modalities were simulated. First, the focus of an unpolarized illuminating field was translated in small increments and the emerging angular spectrum calculated. By calculation of the total power throughput,[28] a point mapping system was simulated, where a large area detector was used and the Cassegrain edges set the limiting apertures in the optical path. That is, the sample was illuminated at a single spot and the transmitted light captured using a single IR detector. Second, widefield illumination with array detection was simulated. The transmitted angular spectrum can be used to calculate the intensity on a detector plane,[29] and for each focal position these intensities can be summed. The fill factor of the detector is not explicitly considered here but the consequences of a nonunity fill factor can be included in the model and are not expected to produce significant qualtitative changes. These two approaches, point mapping and imaging, are both employed in contemporary microspectroscopy, and simulations in Figure 5 for both modalities demonstrate similar results. However, it is instructive to notice how the measured profile of the slab depends on wavenumber. For example, both the gradient of the absorbance at the slab edge and the overshoot at the edge vary with wavenumber. While the wavenumber dependence of the achievable spatial resolution is known,[30] spectral measurements also change with wavelength due to optical effects (such as diffraction and refraction) and, additionally, with sample structure (e.g., thickness). A description of spectral distortions and their effect on spatial specificity (and, in turn, the resolution attainable) is lacking. The model sample of constant $k(\bar{\nu})$ considered here exhibits differing profiles due to wavelength dependent phenomena, emphasizing this relationship between recorded spectra and the apparent morphology of the sample.

Frequency-Variant Samples. To see how optical phenomena influence a measured spectrum, the simulation parameters described for Figure 5 were modified by replacing the constant index of the slab with the complex refractive index of toluene[31] and by replacing the constant index of the substrate by the index of barium fluoride.[32] A background measurement was calculated by applying standard transmission coefficients to model the transmission of light through the air-to-barium-fluoride boundary at the first substrate surface and the barium-fluoride-to-air boundary at the second substrate surface. In the presence of the absorbing toluene slab, both point mapping and imaging profiles were calculated using the methods described above.

Spectra from the imaging modality are shown in Figure 6. In these calculations it was assumed that the pixel size was 5 μm at the sample plane. Spectra are plotted for the center of the slab and for measurements in the vicinity of the edge. It can be seen that light scattered outside of the collection cone produces a nonzero baseline in the measured spectra, as is commonly observed. A smooth baseline function is often fitted to these spectra and subtracted out before spectral metrics are calculated. Here, local linear baselines are fitted to the spectra, as is common practice in spectral preprocessing, and peak position and height metrics calculated (as illustrated in Figure 6). The resulting peak positions are given in Table 1, and the resulting normalized peak heights are given in Table 2. In both cases an ideal value has been calculated by determining the true absorbance profile from the imaginary refractive index.[33]

It can be seen that the observed spectral metrics depend on the position at which the spectra are measured. Optical effects distort the spectra by coupling the real part of the refractive index and the sample structure into the data. While baselining has removed some of the gross optical effects, the metrics are not independent of morphology. It should be noted that correction algorithms other than baseline subtraction have been proposed, e.g., taking derivatives of the spectra or more advanced procedures.[34,35] However, these procedures are typically ad hoc or do not fully account for physical phenomena such as the coupling of the dispersive line-shape (the real index) into the observed spectra and the influence of the sample morphology on the collected data. Hence they cannot capture the physics of the true distortions and may provide unjustified confidence compared to uncorrected data.

The point mapping modality was also simulated, and the measured spectra are shown in Figure 7. While there are differences, the gross behavior can be seen to be similar to that observed in the imaging modality. In this example, the observed peak positions (Table 3) are the same as for the mapping case, while the peak ratio (Table 4) metrics differ but exhibit a similar amount of variability as the imaging case. The baseline characteristics differ between the imaging and mapping modalities. This is to be expected as scattering distorts the point spread function of the light to spatially redistribute light intensity incident on the detector—in imaging mode this means that light scattered from an edge can effect neighboring pixels, while for mapping this type of crosstalk does not occur.

(28) Equation 32 in ref 5.
(29) Equations 30 and 31 in ref 5.
(30) Lasch, P.; Naumann, D. *Biochim. Biophys. Acta* **2006**, *1758*, 814–829.
(31) Figure 6 in ref 5.
(32) Malitson, I. H. *J. Opt. Soc. Am.* **1964**, *54*, 628–632.
(33) Equation 35 in ref 5.
(34) Kohler, A.; Kirschner, C.; Oust, A.; Martens, H. *Appl. Spectrosc.* **2005**, *59*, 707–716.
(35) Thennadil, S. N.; Martens, H.; Kohler, A. *Appl. Spectrosc.* **2005**, *60*, 315–321.

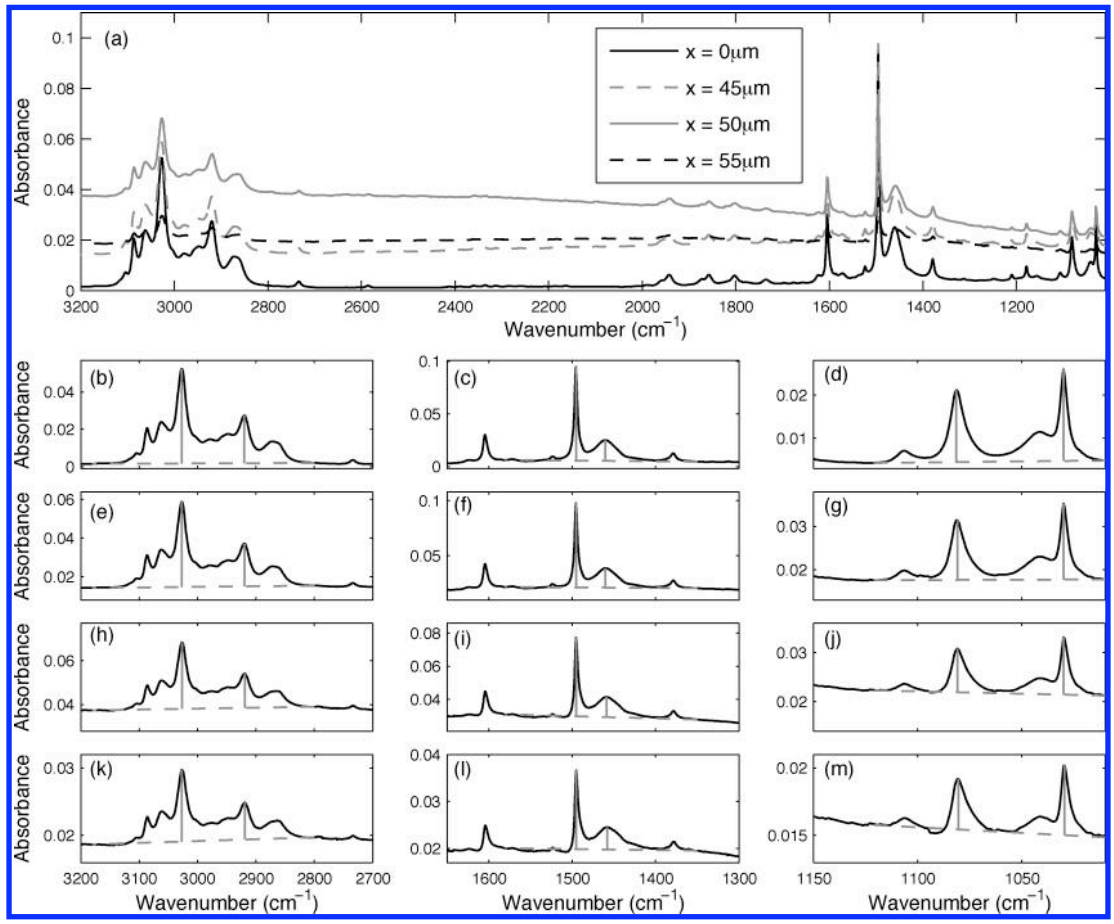

Figure 6. Imaging spectra from a 7 μm thick toluene slab on 2 mm of barium fluoride. The absorbance is normalized by the slab thickness. Spectra are shown from the center of the slab ($x_0 = 0$) and in the vicinity of the edge ($x = 50$ μm). The full spectra (a), and details for $x = 0$ (b−d), $x = 45$ μm (e−g), $x = 50$ μm (h−j), and $x = 55$ μm (k−m) are shown. A baseline is illustrated by a dashed line in the detail plots, and peak heights and positions are calculated as illustrated by the solid vertical lines. The calculated metrics are given in Tables 1 and 2.

Table 1. Peak Positions for the Imaging Data to the Nearest 0.5 cm^{-1}

	peak 1	peak 2	peak 3	peak 4	peak 5	peak 6
ideal	3027.0	2920.0	1495.5	1460.5	1030.0	1081.5
$x_0 = 0$	3027.0	2920.0	1495.5	1460.0	1030.0	1081.5
$x_0 = 45$ μm	3027.0	2919.5	1495.5	1460.0	1030.0	1081.0
$x_0 = 50$ μm	3026.5	2919.0	1495.5	1459.0	1030.0	1081.0
$x_0 = 55$ μm	3027.0	2919.0	1495.0	1458.0	1029.5	1080.5

Table 2. Normalized Peak Heights for the Imaging Data

	peak 1	peak 2	peak 3	peak 4	peak 5	peak 6
ideal	1.00	0.514	1.79	0.436	0.444	0.350
$x_0 = 0$	1.00	0.505	1.76	0.388	0.416	0.327
$x_0 = 45$ μm	1.00	0.505	1.74	0.400	0.401	0.314
$x_0 = 50$ μm	1.00	0.517	1.57	0.401	0.388	0.296
$x_0 = 55$ μm	1.00	0.517	1.58	0.447	0.486	0.352

Note that the severity of the metric distortion depends on the sample morphology and boundaries. For example, Figures S4 and S5 in the Supporting Information show results for a sample thickness of 2 μm rather than 7 μm. It can be seen that optical distortions, such as the nonzero baseline, are less severe for the 2 μm thick sample. As noted earlier, thinner samples can, in general, be expected to be less susceptible to distortions due to optical phenomena than comparable thicker samples. Spectral metrics are also affected to a lesser extent as can be seen by comparing the metric tables for the 2 μm thick sample (Tables S2−S5 in the Supporting Information) to the metric tables for the 7 μm thick samples above. For example, in the latter, a maximum peak shift of 2.5 cm^{-1} is observed, while for a 2 μm thick sample, the maximum peak shift is 1 cm^{-1}.

The dependence of spectral distortions on sample parameters is important from two perspectives. First, the effect of geometry becomes difficult to quantify in simple terms. Hence, a measure of the systematic deviations in the spectrum must be individually calculated for specific samples. This is especially important for studies that are interested in subtle chemical changes at edges (often several wavenumber shifts) or in an algorithm-based search. While careful simulations are prescribed for sensitive chemical analyses, the strategy in database searching may be to use a coarse spectral resolution. Second, in automated analysis algorithms such as those for tissue histopathology,[36] sample thickness becomes an important parameter whose impact must be appreciated. One approach may be to carefully control sample thickness such that deviations are consistent and can be eliminated from use in classification algorithms by choice of appropriate metrics. A second approach is to use a large number of samples with a thickness variation arising from the natural variation of the

(36) Fernandez, D. C.; Bhargava, R.; Hewitt, S. M.; Levin, I. W. *Nat. Biotechnol.* **2005**, *23*, 469–474.

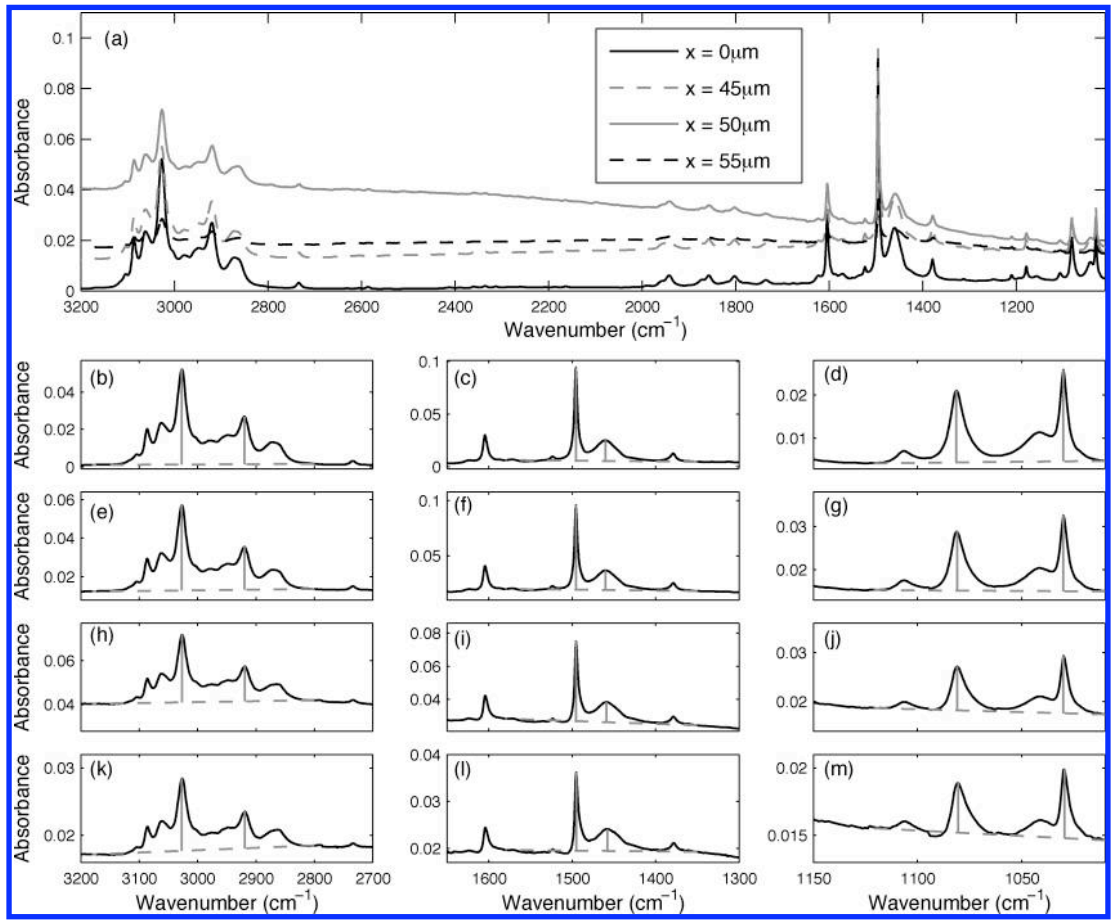

Figure 7. Point mapping spectra from a 7 μm thick toluene slab on 2 mm of barium fluoride. The absorbance is normalized by the slab thickness. Spectra are shown from the center of the slab ($x = 0$) and in the vicinity of the edge ($x = 50$ μm). The full spectra (a) and details for $x = 0$ (b−d), $x = 45$ μm (e−g), $x = 50$ μm (h−j), and $x = 55$ μm (k−m) are shown. A baseline is illustrated by dashed lines, and peak heights and positions are calculated as illustrated by the solid vertical lines. The calculated metrics are given in Tables 3 and 4.

Table 3. Peak Positions for the Point Mapping Data to the Nearest 0.5 cm^{-1}

	peak 1	peak 2	peak 3	peak 4	peak 5	peak 6
ideal	3027.0	2920.0	1495.5	1460.5	1030.0	1081.5
$x_0 = 0$	3027.0	2920.0	1495.5	1460.0	1030.0	1081.5
$x_0 = 45$ μm	3027.0	2919.5	1495.5	1460.0	1030.0	1081.0
$x_0 = 50$ μm	3026.5	2919.0	1495.5	1459.0	1030.0	1081.0
$x_0 = 55$ μm	3027.0	2919.0	1495.0	1458.0	1029.5	1080.5

Table 4. Normalized Peak Heights for the Point Mapping Data

	peak 1	peak 2	peak 3	peak 4	peak 5	peak 6
ideal	1.00	0.514	1.79	0.436	0.444	0.350
$x_0 = 0$	1.00	0.502	1.75	0.386	0.415	0.326
$x_0 = 45$ μm	1.00	0.504	1.73	0.403	0.397	0.309
$x_0 = 50$ μm	1.00	0.520	1.56	0.395	0.382	0.292
$x_0 = 55$ μm	1.00	0.509	1.55	0.435	0.475	0.342

protocol. Any developed classification algorithm then will be insensitive to optics-induced distortions within the range of thicknesses used in the development of the protocol.

Experimental Comparison. To test the predictive power of the model presented here, it is useful to compare experimental data with simulations for a comparable sample and imaging system. The sample data were recorded on a Varian Stingray system using a mid-IR interferometer. The microscope of the instrument is equipped with a narrowband, liquid nitrogen cooled mercury−cadmium−telluride (MCT) detector, as well as a 128 × 128 pixel, liquid nitrogen-cooled focal plane array MCT detector. Data are recorded at an undersampling ratio of 2 referenced to the He−Ne laser, zero-filled by a factor of 2, and Fourier transformed using Happ−Genzel apodization. The nominal spectral resolution was 2 cm^{-1}. The ratios of two similarly collected image sets (one without a sample to serve as a background and one with a sample) are taken pixel by pixel to obtain absorbance image datasets. A common photoresist material, SU-8 2000.5 (MicroChem Corp., Newton, MA), was spin coated to an approximate thickness of 10 μm on a 25 mm diameter barium fluoride (BaF_2) disk and pattern cured by UV exposure using a standard USAF 1951 target (Edmond Optics, Barrington, NJ). The entire sample was baked at 95 C and developed as per standard protocols for postcuring. A postbake at 150 C for 5 min was performed to ensure complete polymerization and long-term stability.

An image of the transmittance, at $\bar{\nu} = 2903$ cm^{-1}, for a region of the target is shown in Figure 8. The data measured along the dashed line will be examined; in particular, the spatial−spectral response across the edge of a bar structure is of interest. The absorbance profile along the dotted line shown in Figure 8 is

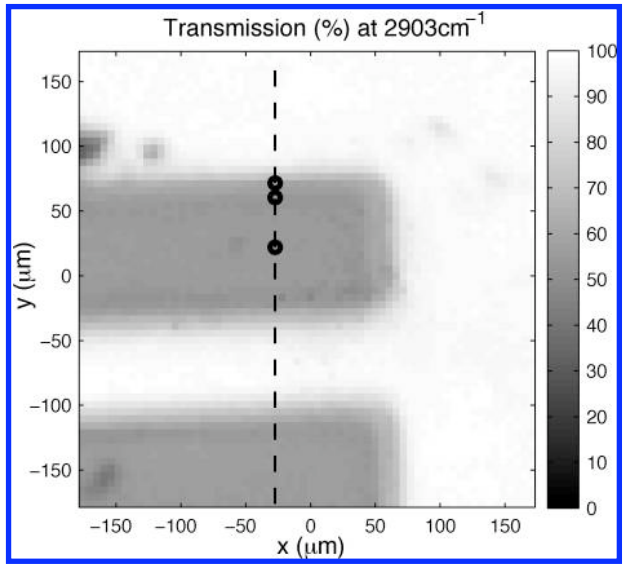

Figure 8. Transmission image of a SU-8 bar target on barium fluoride at 2903 cm^{-1}. In subsequent figures, profiles will be displayed from along the dashed line, and spectra will be plotted for the points marked with a circle.

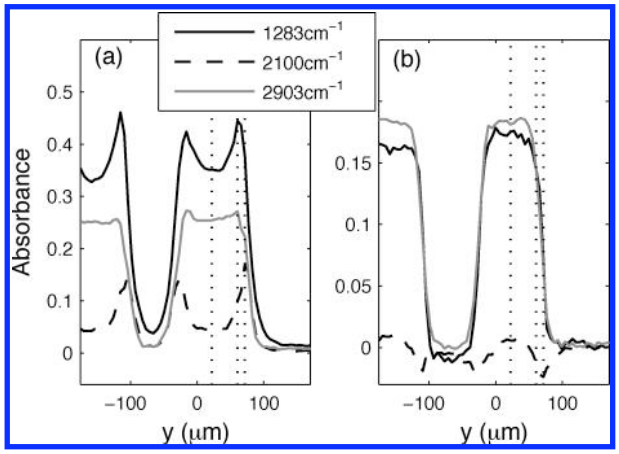

Figure 9. Absorbance profiles, before (a) and after (b) baseline correction, across the bar target for three different wavenumbers. At $\bar{\nu} = 1283$ cm^{-1} and $\bar{\nu} = 2903$ cm^{-1}, the SU-8 polymer is absorbing. At $\bar{\nu} = 2100$ cm^{-1}, the polymer is nonabsorbing but scattering effects produce apparent absorption at the edges.

plotted for three different wavenumbers in Figure 9a. Apparent artifacts, e.g., overshoot in the absorbance at the sample edges, can be seen to vary with wavenumber. These distortions arise from both baseline offset due to redistribution of intensity by the sample and changes in the apparent peak shape. Other wavenumber-dependent effects are also visible, e.g., the change in spatial resolution as a function of wavenumber is manifest in the differing gradients of the absorbance profiles at the edge.

Subtracting a slowly varying baseline is a common method to compensate for the consequences of optical effects on spectra. In Figure 9b, the edge profiles are replotted after a linear baseline has been subtracted from the spectra. For each of the spectra, the baseline was found by linear interpolation between minima of the SU-8 response, specifically between the absorbance values at 910, 1423, 1551, 1827, 2696, 2783, 3111, 3736, and 3931 cm^{-1}. It can be seen that the baselining procedure qualitatively improves the edge profiles, at least in absorbing regions of the

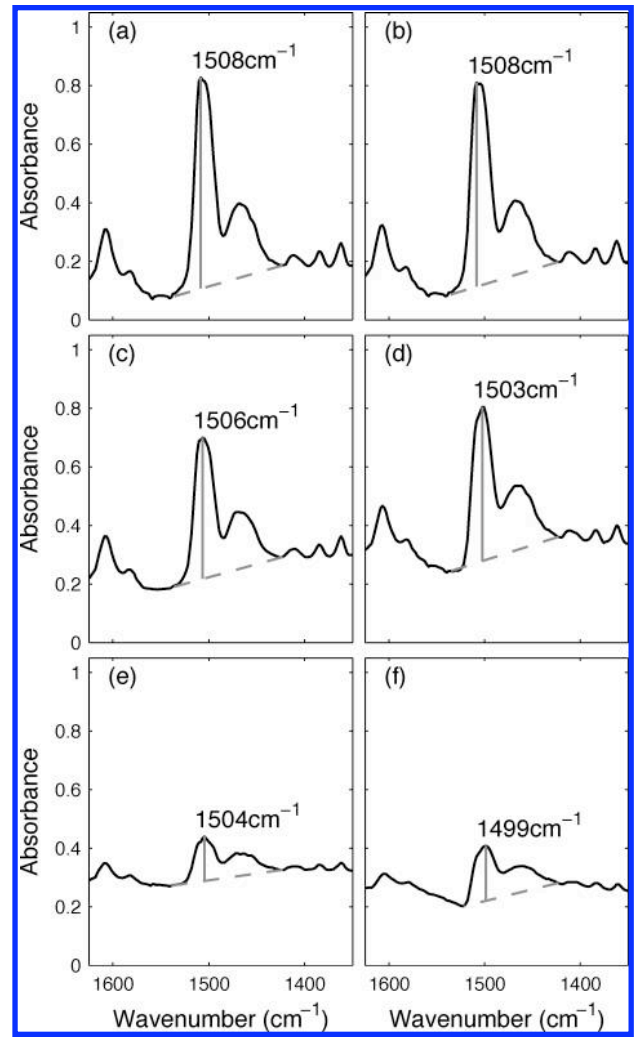

Figure 10. Experimental absorbance spectra taken at $y = 22$ μm (a), $y = 60.5$ μm (c), and $y = 71.5$ μm (e) (i.e., the points marked with a circle in Figure 8) and simulated spectra taken from the polymer 50 (b) and 6 μm (d) from the edge and from off the polymer 5 μm from the edge (f). The peak location, after the illustrated baseline correction, is displayed on the plots.

spectrum. Such subjective baselining can lead to seemingly reasonable results, especially when scattering is high and absorbance is low. For automated analyses, which are required due to the large number of pixels (spectra) making manual correction impossible, simple corrections may lead to errors. For example, at 2100 cm^{-1}, the baselining procedure has resulted in some nonphysical negative values of absorbance. Another potential concern is the discrepancy in absorbance between the two bar targets. For the bar centered around $y = 20$ μm, the absorbance values at 1283 and 2903 cm^{-1} are approximately equal, while the neighboring bar exhibits a greater difference, despite being made of the same material and being subject to the same processing history.

Quantitative examination of the collected data reveals spectral distortions of the type predicted earlier in the article. An illustrative absorption peak is centered around $\bar{\nu} = 1508$ cm^{-1}. Experimental measurements of this peak are shown for various sample locations in the left column of Figure 10. Data collection from this peak can be simulated by first estimating the physical properties of the sample. By comparison of the absorbance

measured at $y = 22$ μm in relation to the imaginary part of the refractive index of SU-8 calculated in the previous article, the thickness of the SU-8 was estimated to be approximately 7 μm. The imaginary part of the refractive index was then estimated from the absorbance[33] (again from the measurement at $y = 22$ μm). Kramers−Kronig[37] analysis was used to calculate the real part of the refractive index, thus completing the description of the object. Note that the SU-8 refractive index calculated in the previous article was not employed, as differences in sample preparation were found to have introduced small but significant differences in the optical properties of the polymer.

The sample edge profile and the instrument were modeled in the same manner used to generate Figure 6, except that the inner and outer numerical apertures of the Cassegrain were taken to be 0.26 and 0.4, respectively. These values are consistent with those used for the same instrument in the previous article. The experimental and predicted spectral profiles of parts a and b of Figure 10 agree well. This is to be expected as the SU-8 refractive index used in the simulations was calculated from Figure 10a, and this region of the sample is a relatively simple layered structure.

In the vicinity of the polymer edge, the peak position in the experimental data can be seen to shift. Since the target structure is made of a single material, this shift can most likely be attributed to optical effects. Nonuniform curing occurring at the sample edges can be ruled out due to extensive postreaction thermal cure. The simulations also predict a peak shift toward lower wavenumber; however, this shift is greater in the predictions than it is in the measurements. There are several possible causes for this overestimation. The characterization of the sample relied on a chain of estimation procedures, the real index was estimated from the imaginary index which was in turn dependent on the assumed sample thickness, with the possibility of propagating errors. The correct prediction of bulk spectra, however, suggests that this error is small. The sample geometry may also lead to errors in prediction. In simulation, the edge is represented by a steep gradient between two perfectly flat surfaces. In reality, the sample edges can be expected to have some finite and unknown slope, and the horizontal surfaces in the bar targets may not be perfectly flat. The broad agreement between the experimental and simulated results of Figure 10 indicate that the model developed has significant predictive power and allows an understanding of the causes and effects of optical artifacts.

(37) Kuzmenko, A. B. *Rev. Sci. Instrum.* **2005**, *76*, 083108.

CONCLUDING REMARKS

This article presents the first attempt at applying rigorous optical theory to heterogeneous samples in IR microspectroscopy. It is shown that lateral structure in thin samples leads to significant effects on the recorded spectral data arising from a coupling between wavelength, sample geometry, optical properties within the sample, presence of interfaces, and the optical setup. With the use of progressively sophisticated simulations, the effect of each of these factors was demonstrated in a quantitative manner. It was shown that the redistribution at the detector place of the intensity incident upon the sample can be quantitatively modeled and verified with experiments. The implications for the practice of spectroscopy are that the spatial and spectral variation of the real and imaginary parts of the index of the sample cannot be decoupled from FT-IR imaging data, as is currently practiced. It is emphasized that recording the true data will require the development of both new instruments that can provide additional data to extract true spectral properties from the data, as well as numerical methods to assist in the same. The theoretical framework presented here should serve as a useful guide to estimate the true structure and quantify distortions in present instruments as well as a platform for future development.

ACKNOWLEDGMENT

This work was supported in part by the Grainger Foundation for Emerging Technologies, the Department of Defense Prostate Cancer Research Program, and Susan G. Komen for the Cure. The authors would also like to thank Dr. Gokulakrishnan Srinivasan for fabricating the SU-8 sample and Dr. Michael J. Walsh for help in acquiring data.

SUPPORTING INFORMATION AVAILABLE

Additional information as noted in text. This material is available free of charge via the Internet at http://pubs.acs.org.

Received for review September 15, 2009. Accepted December 31, 2009.

AC902068E